CAPÍTULO 4

Deep Learning-Based Jaszczak ACR Phantom Segmentation for Optimized Radium-223 Dosimetry

Cristian F. Griebler[a], Luis Felipe C. Lima[b], Leanderson P. Cordeiro[c], Wagner Bolzan[d], Lidia V. De Sá[a], Daniel A. B. Bonifacio[a]

[a]*Radioprotection Dosimetry Institute (IRD), Brazil*
[b]*Nuclear Instrumentation Laboratory (COPPE,UFRJ)*
[c]*Federal University of Pernambuco (UFPE), Brazil*
[d]*Bionuclear Clinic, Brazil*

Abstract

Precise and personalized absorbed dose estimation in radionuclide therapy is crucial for optimizing treatment efficiency while minimizing harm to healthy tissues. Radium-223 dichloride (Ra-223), an alpha emitter used in treating metastatic castration-resistant prostate cancer (mCRPC), has shown positive results in extending patient survival. However, the current practice of uniform Ra-223 activity administration based solely on patient weight can lead to suboptimal treatment outcomes. Evaluating treatment efficacy involves quantifying activity and absorbed dose through image quality analysis, revealing potential areas for optimization in patient outcomes. This work introduces an innovative approach that combines a deep learning-based model for automated segmentation of the Jaszczak ACR phantom—a tool for image quality analysis in nuclear medicine—with Monte Carlo simulation for dosimetry. The model exhibits efficient segmentation, surpassing 91.2% in class-wise Dice coefficients, offering a time-efficient alternative to manual segmentation. The study underscores the superior performance of the 89 keV energy window in image quality parameters, emphasizing its role in lesion detection. Furthermore, the investigation sheds light on the nuanced challenges associated with accurate quantitative outcomes in nuclear medicine applications, particularly in the context of Ra-223 therapy. In conclusion, this study contributes insights into refining dosimetry protocols for Ra-223, enhancing the precision of quantitative outcomes in nuclear medicine. The practical implications extend to improving daily routines for clinical professionals involved in nuclear medicine applications, showcasing the potential of advanced imaging techniques and computational tools in optimizing Ra-223 therapy.

Introduction

In nuclear medicine, precise and personalized estimation of absorbed dose delivery to specific target areas plays an essential role [1]. Radium-223 (Ra-223) has emerged as a promising radiopharmaceutical for the treatment of metastatic castration-resistant prostate cancer (mCRPC) [2]. Ra-223, an alpha emitter that mimics calcium, exhibits an affinity for regions characterized by elevated bone turnover, often associated with bone metastases [2]. Its selective targeting of bone lesions and the emission of alpha particles makes it a powerful tool for managing this debilitating condition. Nevertheless, the evaluation of Ra-223 therapy depends on precise and personalized dosimetry, which is critical for optimizing therapeutic efficacy while minimizing radiation exposure to healthy tissues [2,3].

One of the significant advantages of Ra-223 is its minimal toxicity towards surrounding tissues, especially the bone marrow, which can be attributed to the limited range of the alpha particles it emits [2,4]. Significantly, the administration of Ra-223 has shown impressive results, extending the overall survival of patients suffering from castration-resistant prostate cancer and bone metastases, with a remarkable 30% reduction in the risk of mortality [4,5].

Currently, Ra-223 activity administration is solely determined by patient weight at a rate of 55 kBq/kg, with no consideration given to the patient's physical or morphological attributes. This uniform activity prescription results in fluctuating absorbed doses within normal organs and target tissues among different patients and even within distinct lesions within the same patient [6, 7]. As a result, this weight-based approach has the potential to lead to suboptimal or excessive treatment, running counter to the optimization principle required by the European Council Directive (2013/59/EURATOM) [9]. Nevertheless, its therapeutic effectiveness and potential side effects are intricately tied to the precise assessment of the absorbed dose within target regions and organs at risk [1,8]. To obtain this objective, the incorporation of advanced imaging techniques and computational dosimetry tools are imperative [1,5,8].

Single-photon emission computed tomography combined with computed tomography (SPECT/CT) enables hybrid imaging that allows for the precise localization of radiopharmaceutical distribution and quantification process. Accurate imaging quantification

requires precise and efficient segmentation of Volumes of Interest (VOIs) to perform Image quality analysis [10,11]. This analysis can be performed in different medical imaging modalities using Jaszczak ACR phantom [10,11].

To address the demand for efficient segmentation, this work introduces a deep learning-based model designed for the automated segmentation of the Jaszczak ACR phantom. This model leverages the capabilities of artificial intelligence for automated segmentation, thereby optimizing efficiency and consistency [12,13]. This enhancement in segmentation processes further refines quantification determinations, making a substantial contribution to dosimetry assessments.

In this paper, we present an integrated approach that combines a deep learning-based model for Jaszczak ACR phantom segmentation and Monte Carlo simulation for dosimetry. The focus is on evaluating the impact of recovery coefficient correction on dosimetry assessments, providing valuable insights into this methodology to enhance the precision of Ra-223 quantification.

Materials and Methods

Imaging procedures were conducted using the Symbia T2 SPECT/CT equipment (Siemens Medical Solution Inc., USA) with a medium-energy general-purpose (MEGP) collimator, as recommended in previous studies [14,15].

Jaszczak ACR phantom

The study employed the Jaszczak ACR phantom for image quality analysis. The Jaszczak ACR phantom comprises four fillable plastic cylinders designed to mimic lesion uptake, with volumes of 2, 4.5, 8 and 19 ml and corresponding diameters of 8, 12 , 16 and 25 mm. Additionally, three supplementary cylinders, each with a 19 ml volume, were incorporated into the phantom, composed of varying materials to simulate bone tissue (Teflon), water-filled plastic, and air-filled plastic. The total volume of the Jaszczak ACR phantom, inclusive of all cylinders, amounts to 6.815 liters [16].

Administered Activity

Accordingly to the pharmaceutical company [17], up to 77% of the administered activity is absorbed by the bone tissue, leaving the remaining 23% circulating throughout the body. Considering the prescribed radiopharmaceutical dosage of 55 kBq/kg [17] and taking into account the total volume of the Jaszczak phantom (6,815 L), the activity to be administered is 374.82 kBq.

Relying on the proportion of absorption by bone tissue, the experimental activity concentration within the cylinders was 8.14 kBq/mL, while it was 0.0179 kBq/mL within the simulator body. In the sensitivity test, the approximate experimental activity introduced into the syringe was 8.14 kBq/mL as well.

Image Reconstruction

The acquisition protocol encompassed energy windows set at 89 keV (with a 24% width), 154 keV (with a 20% width), 270 keV (with a 20% width), and a triple energy window configuration. The SPECT system employed a circular orbit with a 2.8125° rotation step at 30-second intervals, totaling 180° with 64 views for each head. This configuration was chosen to ensure a balanced photon statistics profile and a feasible total acquisition time of 32 minutes for prospective patient studies. The acquired images were reconstructed with a matrix size of 128 × 128, maintaining a high-resolution representation.

Image reconstructions were performed using OSEM/MLEM with 8 subsets with 4 iterations based on a previous study [14]. A Gaussian filter with 4 mm FWHM (full width at half maximum) was applied. Attenuation correction was performed through attenuation maps obtained from the CT acquisition.

Deep Learning-Based Jaszczak ACR Phantom Segmentation

A set of 26 CT images were used for the model training, with a set of five CT images employed specifically for synthetic data generation. To enhance dataset diversity and increase the robustness of our model, data augmentation techniques were applied [18]. These techniques involve the processes of rotation, translation, and flipping to create synthetic data points. The acquisition of the original data was performed using the Symbia T2 Siemens SPECT/CT equipment.

For the training process, we used MONAI Label [13] in conjunction with Slicer 3D software [19]. The MONAI Label tool provides support for automated segmentation as an annotation approach, primarily leveraging a noninteractive algorithm based on a standard convolutional neural network (CNN), such as UNET [20], nnU-Net [21] or UNETR [22]. In contrast, Monai offers an interactive segmentation model, DeepGrow, in which the user actively participates by providing positive and negative clicks. Positive clicks are employed to expand the segmentation to include areas of interest, whereas negative clicks are utilized to contract the segmentation by excluding specific regions from the area of interest [13].

DeepEdit extends the concept of DeepGrow's click-based segmentation by enabling both click-free segmentation inference and click-based segmentation editing [12]. Notably, the key distinctions lie in how this model is trained and the composition of the input tensor's channels. During the training process, the input tensor can take one of two forms: It can either consist of the image with zeroed tensors in automatic segmentation mode, or it may incorporate tensors representing user-provided label and background clicks in interactive mode [12].

The DeepEdit model's algorithms were adapted to recognize five distinct labels corresponding to the structure of the ACR phantom using . These labels include four designations for the fillable cylinders, which are referred to as cylinder 1, 2, 3, and 4, as well as a background label.

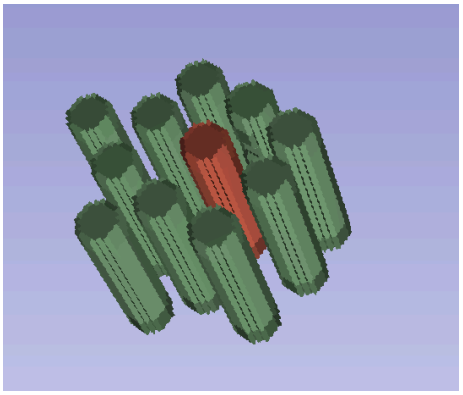

Figure 1. Volume rendered in Slicer 3D for image quality analysis. Ten green cylinders for background counts and the red cylinder for targeted count

The dataset comprised 26 CT images, and we implemented a split ratio of 0.2. As a result, 21 images were designated for the training phase, while the remaining 5 images were set aside for evaluation. All 26 images used in the model were manually labeled using the Segment Editor tool in Slicer 3D [19] . The used optimizer was Adam with 0.001 initial learning rate.

We employed the Dice coefficient and mean Dice as key metrics to evaluate the accuracy of the model [13]. These metrics have been adopted in the field of medical image analysis for their efficacy in quantifying the overlap between predicted and ground truth segmentations [12].

Sensitivity Test

A sensitivity test was conducted to evaluate the system's responsiveness to varying input activities. This involved injecting a known activity (8.14 kBq/mL) into the 8 ml syringe to simulate a lesion, allowing for the quantitative assessment of the system's ability to detect and quantify low activity levels.

Image Quality Analysis

Image quality analysis was undertaken to assess the following reconstruction parameters: Contrast (C_i) , Signal-to-Noise Ratio (SNR_i), and Recovery Coefficient (RC). Volumes-of-Interest (VOIs) were delineated with diameters corresponding to the physical inner diameters of the four hot cylinders through the deep learning-based Jaszczak ACR Phantom segmentation. or each VOI size, 10 VOIs were designated to obtain background counts to ensure a consistent background noise metric across all four hot cylinders. Figure 1 illustrates the (VOIs for image quality analysis of a cylinder with 8 mm of diameter. The SNR_i and Contrast (C_i) values for each hot cylinder and each energy window configuration were calculated. The SNR_i and C_i are defined as

$$SNR_i = (P_i - B_i) / D_i$$

$$C_i = P_i / B_i$$

where D_i represents the standard deviation value within the background (BG) circle corresponding to the *ith* BG circle, B_i denotes the average count value within the BG circle associated with the *ith* cylinder and P_i is the average count value within the *ith* cylinder.

Furthermore, to quantify the sensitivity of the equipment and the contribution of each energy window, we used a syringe with 8 ml of volume filled with a solution of 8.14 kBq/ml of Ra-223 as a lesion simulator. The sensitivity is defined as

$$S_i = \left(\frac{Counts}{A*t}\right),$$

where Counts is the total number of counts measured in a VOI within the radioactive volume; t is the acquisition duration (seconds); and A is the activity in the cylinder (kBq). According to the MIRD pamphlet 22 [23], the RC is used to study the accuracy of activity quantification in SPECT/CT images. The RC is defined as:

$$RC = (A_{det\,i} - A_{det,\,BG\,i}) / (A_{ins\,i} - A_{ins,\,BG\,i})$$

where $A_{det\,i}$ is the identified activity within the *ith* cylinder, $A_{det,\,BG\,i}$ is the background activity detected within a cylinder of the *ith* volume, $A_{ins\,i}$ is the actual activity present inside the *ith* cylinder and $A_{ins,\,BG\,i}$ is the genuine background activity within a cylinder of the *ith* volume and a specified background activity concentration. For example, the activity estimated for the 89 keV energy window is:

$$A_{det\,i} = \left(\frac{C_{measured}}{S_{89\,keV} * t}\right)$$

Because spatial resolution degrades as collimator-to-patient distance increases, the protocol distance from phantom image acquisition was the same as patient image acquisition. The functionality of automated border contour was activated during the images acquisitions.

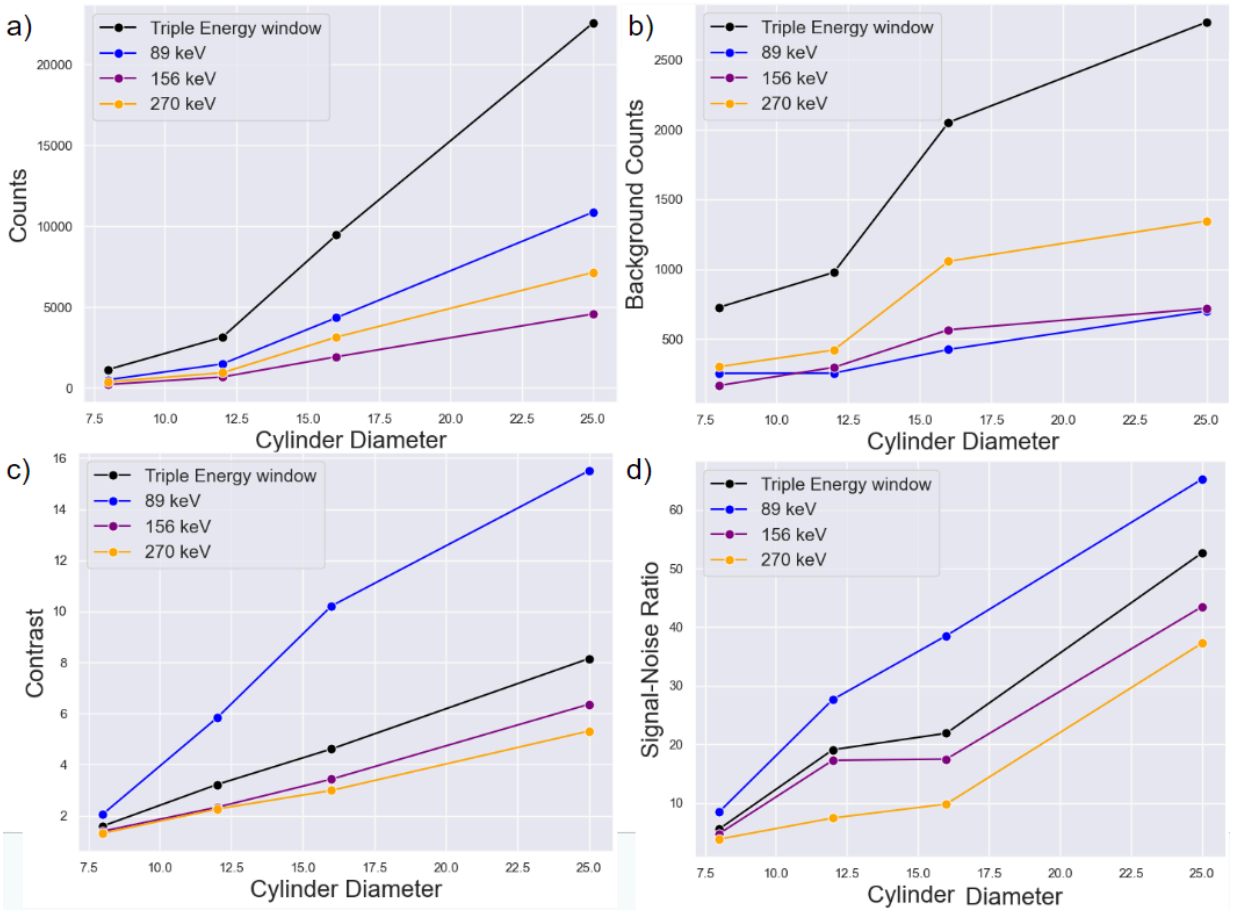

Fig. 2. Image quality parameters. a) Average counts inside each cylinder b) average counts inside background cylinders c) Contrast versus cylinder diameter size d) Signal-Noise-Ratio versus cylinder diameter size.

Dosimetry

The dosimetry study employed GATE(GEant4 Application for Emission Tomography) version 9.3 in conjunction with Geant4(GEometry and Tracking) version 11.1 [24]. GATE inherits electromagnetic physics processes constructors from Geant4, with a set of predefined Physics Lists (PL). For this research, PL Standard Option 3 was used, loading physics processes definitions recommended for medical physics applications [24]. This option defaults to the distance-to-boundary setting and specifies 220 bins for stopping power and mean free path tables [24].

The simulation also encompassed the phantom geometry and its materials, as well the Ra-223 source distribution [25]. Dose values were derived from 3D maps generated as the output of the GATE dose actor [26]. The simulated time was set to a 30-minute acquisition period using the command 'setTimeStop 1800s'. The simulation encompassed approximately $5 * 10^8$ events. Dosimetric evaluations were based on activity data extracted from the 89 keV energy window, considering both scenarios with and without recovery correction (RC), and were compared with the ground truth dosimetry derived from the inserted activity in the cylinders.

Results

The SPECT image of the 8 ml syringe was captured for sensitivity evaluation. The 89 keV energy window (with a width of ±24%) exhibited the highest contribution to the recorded counts, representing 53.82% of the total. Subsequently, the 156 keV (20%) and 270 keV (20%) energy windows contributed 18.75% and 27.43%, respectively.

The Counts (Figure 2a) indicate the number of detected counts according to cylinder diameter size. In Figure 3b, background counts correspond to the average counts measured within each background VOI. The triple energy window combines counts from three energy windows, so both counts and background counts would be higher compared to the other energy windows.

Notably, across all four cylinder volumes, the 89 keV energy window exhibited higher count values and lower background counts than the 156 keV and 270 keV energy windows, impacting both Contrast and SNR performance. The contrast of the 89 keV energy window displays a significant difference for cylinder diameters exceeding 12 mm when compared to other energy windows, as illustrated in Figure 2c.

In particular, the 270 keV energy window exhibited higher background count values compared to the 156 keV and 89 keV energy windows, leading to the lowest SNR values for all cylinders (see Figure 2d). Conversely, the 89 keV energy window displayed superior performance, yielding the highest SNR compared to alternative energy windows.

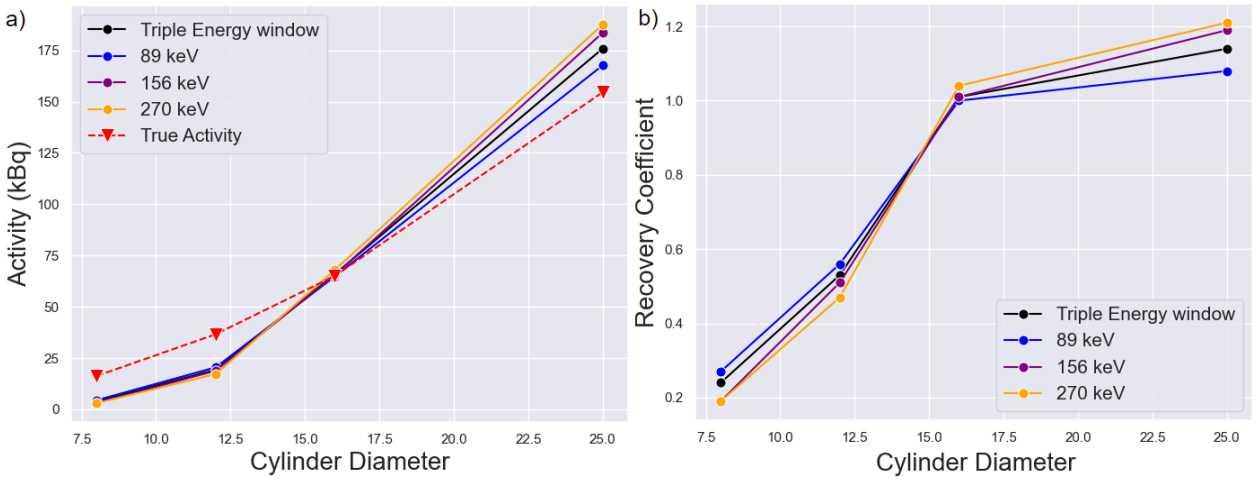

Fig. 3. Activities and Recovery Coefficient. a) Detected activities and inserted activity inside each cylinder b) Recovery coefficient of each energy window and cylinder size.

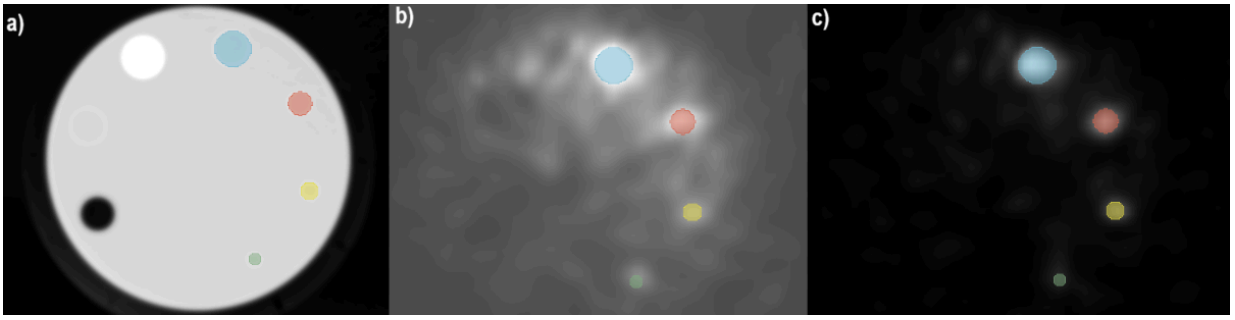

Fig. 4. Automatic segmentation by deep learning-based model. a) Generated segmentation in CT image. b) Applied segmentation in SPECT image of triple energy window. c) Applied segmentation in SPECT image of 89 keV energy window.

To determine the RC, the detected activity was measured across cylinder volumes and energy windows, as illustrated in Figure 3a. The RC serves as a quantification of the disparity between the detected and inserted activity within each cylinder. Notably, the RC for the 25mm cylinder ranges from 1.08 for the 89 keV window to 1.21 for the 270 keV window. These findings suggest that the activity of 25mm lesions may be overestimated by up to 8± 1.4%.

Contrarily, an RC value less than one shows a partial volume effect, as observed in the 8mm and 12mm cylinders in Figure 3b. Specifically, the RC for the 12mm cylinder ranges from 0.56 for the 89 keV energy window to 0.47 for the 270 keV energy window, while the 8mm diameter cylinder exhibits RC values from 0.27 for the 89 keV energy window to 0.19 for the 156 and 270 keV energy window. These observations imply that the activity of 12 and 8mm lesions may be underestimated by up to 44 ± 8.9% and 73 ± 6.8%, respectively.

Deep Learning-Based Jaszczak ACR Phantom Segmentation

The deep learning model achieved reasonable performance after 500 epochs of training, reaching 10,500 iterations. The best overall metric achieved during training was a Dice coefficient of 0.9717, which occurred at epoch 492, indicating an applicable performance. The specific class-wise Dice coefficients for the training set, such as "cylinder1", "cylinder2", "cylinder3" and "cylinder4" ranged from 0.9210 to 0.9691, demonstrating high accuracy in segmenting these objects.

In the evaluation phase, the model achieved a mean Dice coefficient of 0.9371, with class-wise Dice coefficients ranging from 0.9123 to 0.9232. The best overall evaluation metric was a Dice coefficient of 0.9654, occurring at epoch 483. These results highlight the model's robust performance in segmenting the cylinders in the given dataset, showing promising potential for practical applications.

Dosimetry

Through the examination of dosimetry, Table 1 presents the fluctuations and corrections in both detected activity and dosimetric parameters across cylinder sizes.

Table 1 shows information on cylinder size, detected activity concentration (A_{det}), activity concentration corrected with recovery coefficients (A_{det}^{RC}), absorbed dose of A_{det} (D_{abs}), absorbed dose of A_{det}^{RC} (D_{det}^{RC}), and the true dose calculated from the actual activity inserted into the cylinders (D_{True}).

Table. 1. Results of 89 keV energy window dosimetry.

Cylinder Size	A_{det} **(kBq)**	A_{det}^{RC} **(kBq)**	D_{abs} $(10^{-2}$ **Gy)**	D_{abs}^{RC} $(10^{-2}$ **Gy)**	D_{True} $(10^{-2}$ **Gy)**
25 mm	165.54	152.64	5.29 (0.72)	4.88 (0.67)	4.95 (0.68)
16 mm	64.53	64.84	5.04 (0.69)	5.05 (0.70)	5.08 (0.69)
12 mm	20.01	35.79	2.77 (0.30)	4.95 (0.53)	5.07 (0.54)
8 mm	4.26	15.62	1.32 (0.14)	4.85 (0.50)	5.05 (0.53)

When computing absorbed doses for bone metastatic lesions in SPECT images, it is essential to correct activity detection by applying the suitable recovery coefficient. The results of Table 1 imply that lesions with a size of 25 mm might be overestimated by 8%. In contrast, lesions measuring 12 mm and 8 mm could potentially be underestimated by 44% and 73%, respectively.

Discussion

This study employed the same matrix size, 128 x 128, as previous studies [14,15, 27, 28] to maintain consistency. Opting for a smaller matrix would have sacrificed spatial resolution, while a larger matrix would have resulted in reduced contrast and increased noise [14]. Studies have employed a diverse array of Ra-223 concentrations, from 0.05 µCi/ml [16] to 0.75 µCi/ml [15, 28]. In line with the established medical protocol [17], this study utilized a concentration of 0.25 µCi/ml, consistent with the approach adopted by Lima et al. [14].

In this work, the MEGP collimator was used such as in previous studies [15, 28]. Nonetheless, Owaki *et al* [16] found the HEGP collimator to outperform the MEGP in lesion recognition, especially when evaluating the number of lesions detected during SPECT examinations with Tc-99m HMDP. Also, LEHR (Low Energy High Resolution) collimator has been proved able to visualize and quantify image quality parameters [14]. It's worth noting that the clinical setting where these measurements were conducted did not have access to the HEGP or LEHR collimator.

The application of a Gaussian filter in the study has demonstrated enhancement in the consistency of activity concentration measurements [10]. However, the results of SNR indicate that the use of a Gaussian filter may lead to a decrease in image quality for energy windows of 154 keV and 270 keV, where low count statistics are observed. Additionally, Lima et al [14] reported that Gaussian filters resulted in relative differences when compared to the 89 keV window. Therefore, while a Gaussian filter with a Full Width at Half Maximum (FWHM) of 4 mm can be employed for the 89 keV (+24%) energy protocol, it is not recommended for use in the triple energy window configuration.

The selection of energy windows for capturing Ra-223 emissions in clinical applications has been a topic of debate within the literature [14 - 16, 27]. While certain studies have employed 82 keV ± 20% [15, 28, 29], 84 keV ± 20% [16, 30] or 85.0 keV ± 20% [15], previous research [14, 27] has demonstrated the advantages of adopting the 89 keV photopeak with a 24% width window. This particular energy window is aligned with emitted photons characterized by emission probabilities exceeding 1% [14] and effectively avoids the emission of characteristic X-rays from lead, which occur at 72 and 75 keV with probabilities of 27.7% and 46.2%, respectively [27].

At a concentration of 8.14 kBq/ml within an 8 ml cylinder, a sensitivity of 62.54 ± 5.3 counts per second per megabecquerel (cts/s/MBq) was observed. This result aligns with a prior study by Benabdallah *et al*. [15], where, in the Ra-223 concentration range of 6.5 kBq/ml to 22.8 kBq/ml, sensitivities were reported in the range of 73.7 ± 6.2 to 43.4 ± 5.6 cts/s/MBq.

The contrast parameter at 89 keV exhibited a notable distinction compared to other energy windows, as illustrated in Figure 2c. Moreover, 89 keV demonstrated superior performance across all cylinder sizes when evaluated for the SNR parameter, a crucial metric for energy window selection in lesion detection, given its reliance on differentiation from the background medium. Consequently, the 89 keV window emerged as the optimal choice, offering the most favorable image quality parameters.

In our investigation, the RC for the 25 mm cylinder ranged from 1.08 to 1.21 across different energy windows, suggesting a potential overestimation of up to 8% in the activity of these lesions. This aligns with other references [31, 32], which also observed an overshoot in RC values higher than 1, attributed to the resolution recovery algorithm used during reconstruction, emphasizing its role in influencing quantitative outcomes.

On the other hand, our study highlights a partial volume effect for smaller lesions, specifically the 8mm and 12mm cylinders, with RC values less than 1.0. In contrast, Benabdallah *et al* [15] discusses the RC for 5.6 ml spheres, with background activity, which were mainly overestimated. This discrepancy is attributed to the spill-in and spill-out effects, emphasizing the impact of background activity that, unlike our methodology, was not reduced from the VOIs of the spheres [15].

Besides, for smaller cylinders (12 and 8 mm), the image quality parameters deprecated due to partial volume effects. In a related study [29], an average lesion size of 87 ml (across 53 lesions ranging from 1.2 to 270 ml in 14 patients) was reported for osteoblastic bone metastasis of prostate cancer. Accordingly, we anticipate that our protocol will facilitate the quantification of osteoblastic bone metastasis with clinical uptake. However, it is acknowledged that implementing partial volume correction through RC will be imperative for achieving a more reliable quantification.

A thorough 20-year literature review shows that error rates for clinically significant or major errors in radiology usually range from 2% to 20%, depending on the specific radiological study [33]. Implementing systematic improvements, such as automatic segmentation, has the potential to significantly reduce these error rates.

Manual segmentation of Jaszczak ACR Phantom can take 15 to 30 minutes for experienced and non-experienced clinical professionals, respectively. In

contrast, using deep learning-based segmentation reduces the process to just 2.5 minutes—30 seconds for segmentation and an additional 2 minutes for inspection and correction. This represents a significant time improvement, making it six times faster for experienced professionals and twelve times faster for non-experienced ones.

The deep learning-based Jaszczak ACR Phantom segmentation performance, in the evaluation phase, surpassed 91,23% in class-wise Dice coefficients. The Dice coefficient serves as the main metric for segmentation models validation and performance interpretation [34]. The ability for clinical experts to make real-time adjustments to the segmentation ensures that the model's output aligns with specific clinical needs and purposes. This dynamic interaction enhances the practicality and adaptability of the segmentation tool in a clinical setting, where customization and fine-tuning are often necessary for optimal results.

In addition to its high performance in ACR Phantom segmentation, the potential applicability of the model to various medical imaging modalities such as SPECT [15], PET [35], and MRI [36] highlights its role as a valuable tool for medical image analysis tasks. The interactive mode not only allows clinical professionals to adapt the segmentation to specific purposes but also opens the door for their active contribution to model improvement. The ability for clinical experts to provide corrections to automatic segmentation and then retrain the model with these new annotations fosters a collaborative approach to refining and enhancing the model's performance.

In dosimetry analysis, 25mm cylinder size, indicates a 8,45% difference between A_{det} and A_{det}^{RC}, as well as between $D_{abs}$and D_{abs}^{RC}, emphasizing the impact of the reconstruction technique on the measured activity. The associated variations in dose values further underscore the importance of carefully considering the impact of reconstruction techniques when interpreting results in the context of image quantification.

For smaller cylinder sizes, the percentage difference between D_{abs} and D_{abs}^{RC} became more pronounced due to the partial volume effect. Overall, these results highlight the importance of considering and applying recovery correction, especially in scenarios involving smaller structures, to enhance the accuracy of both activity concentration and absorbed dose estimations in nuclear medicine applications.

Future research in the field should prioritize advancing techniques for mitigating partial volume effects, particularly in the context of smaller lesions. Additionally, the development of targeted strategies to enhance error reduction and workflow efficiency remains a crucial area for exploration. The continued focus on systematic improvements, including the integration of automated segmentation and artificial intelligence technologies, promises to significantly reduce error rates in radiological studies. This dual emphasis on partial volume effect mitigation and workflow efficiency holds substantial potential for elevating the reliability of nuclear medicine analyses, contributing to more accurate and padronized clinical applications.

Conclusion

In conclusion, our thorough dosimetric analysis of diverse cylinder sizes has provided valuable insights into the influence of Recovery Coefficient (RC) on measured activity and absorbed dose values. The study has elucidated discernible patterns in the outcomes related to detected activities, underscoring the crucial significance of RC correction, particularly in the context of smaller structures. The observed variations in dose values further accentuate the imperative need for meticulous consideration when interpreting results within the realm of image quantification.

Our investigation has shed light on the impact of different energy windows on image quality parameters, with the 89 keV energy window consistently demonstrating superior performance compared to its counterparts. While the reconstruction method showcased potential overestimation for larger lesions, the manifestation of partial volume effects in smaller lesions underscores the nuanced challenges inherent in achieving accurate quantitative outcomes in the field of nuclear medicine applications. Additionally, the study introduced a deep learning-based segmentation model for ACR Phantom segmentation, showcasing its potential applicability across various medical imaging modalities and its enhanced efficiency and adaptability in a clinical setting.

In summary, our findings underscore the role of recovery correction in elevating the accuracy of both activity concentration and absorbed dose estimations. This study not only contributes significant insights to the refinement of dosimetry protocols for Ra-223 in nuclear medicine but also offers practical implications for improving the precision of quantitative outcomes, especially in scenarios involving structures of varying sizes.

References:

[1] Danieli R, Milano A, Gallo S, Veronese I, Lascialfari A, Indovina L, Botta F, Ferrari M, Cicchetti A, Raspanti D, Cremonesi M. Personalized Dosimetry in Targeted Radiation Therapy: A Look to Methods, Tools and Critical Aspects. J Pers Med. 2022 Feb 2;12(2):205. doi: 10.3390/jpm12020205. PMID: 35207693; PMCID: PMC8874397.

[2] Morris, M.J., Corey, E., Guise, T.A. et al. Radium-223 mechanism of action: implications for use in treatment combinations. Nat Rev Urol 16, 745–756 (2019). https://doi.org/10.1038/s41585-019-0251-x

[3] Deshayes E, Roumiguie M, Thibault C, Beuzeboc P, Cachin F, Hennequin C, et al. Radium 223 dichloride for prostate cancer treatment. Drug Des Devel Ther. 2017;Volume 11:2643–51. https://doi.org/10.2147/DDDT.S122417.

[4] Parker C, Nilsson S, Heinrich D, Helle SI, O'Sullivan JM, FossåSD, et al. Alpha emitter radium-223 and survival in metastatic prostate cancer. N Engl J Med . 2013. doi: 10.1056/NEJMoa1213755 .

[5] Higano CS, George DJ, Shore ND, Sartor O, Miller K, Conti PS, Sternberg CN, Saad F, Sade JP, Bellmunt J,

Smith MR, Chandrawansa K, Sandström P, Verholen F, Tombal B. Clinical outcomes and treatment patterns in REASSURE: planned interim analysis of a real-world observational study of radium-223 in metastatic castration-resistant prostate cancer. EClinicalMedicine. 2023 May 18;60:101993. doi: 10.1016/j.eclinm.2023.101993. PMID: 37251627; PMCID: PMC10209672.

[6] Sgouros, G.; Kolbert, K.S.; Sheikh, A.; Pentlow, K.S.; Mun, E.F.; Barth, A.; Robbins, R.J.; Larson, S.M. Patient-Specific Dosimetry for 131 IThyroid Cancer Therapy Using 124I PETand3-Dimensional-Internal Dosimetry(3D-ID) Software.J.Nucl.Med.2004,45, 1366–1372.

[7] Sandström,M.;Freedman,N.;Fröss-Baron,K.;Kahn,T.;Sundin,A.Kidney Dosimetry in 777 Patients during 177Lu-DOTATATE Therapy: Aspects on Extrapolations and Measurement Time Points. EJNMMI Phys.2020, 7,1–15.

[8] Pinto GM, Bonifacio DAB, de Sá LV, Lima LFC, Vieira IF, Lopes RT. A cell-based dosimetry model for radium-223 dichloride therapy using bone micro-CT images and GATE simulations. Phys Med Biol. 2020 Feb 12;65(4):045010. doi: 10.1088/1361-6560/ab6b42. PMID: 31935695.

[9] Council E.U. European Council Directive 2013/59/Euratom on Basic Safety Standards for Protection against the Dangers Arising from Exposure to Ionising Radiation and Repealing Directives 89/618/Euratom, 90/641/Euratom, 96/29/ Euratom, 97/43/Euratom and 2003/122/Euratom. Off. J. Eur. Union. 2014;L13:1–73

[10] Dickson, J.C., Armstrong, I.S., Gabiña, P.M. et al. EANM practice guideline for quantitative SPECT-CT. Eur J Nucl Med Mol Imaging 50, 980–995 (2023). https://doi.org/10.1007/s00259-022-06028-9.

[11] Gear JI, Cox MG, Gustafsson J, Gleisner KS, Murray I, Glatting G, Konijnenberg M, Flux GD. EANM practical guidance on uncertainty analysis for molecular radiotherapy absorbed dose calculations. Eur J Nucl Med Mol Imaging. 2018 Dec;45(13):2456-2474. doi: 10.1007/s00259-018-4136-7. Epub 2018 Sep 14. PMID: 30218316; PMCID: PMC6208822.

[12] Diaz-Pinto, A., et al.: DeepEdit: deep editable learning for interactive segmentation of 3D medical images. In: Nguyen, H.V., Huang, S.X., Xue, Y. (eds.) Data Augmentation, Labelling, and Imperfections: Second MICCAI Workshop, DALI 2022, Held in Conjunction with MICCAI 2022, Singapore, 22 September 2022, Proceedings, pp. 11–21. Springer, Cham (2022). https://doi.org/10.1007/978-3-031-17027-0_2

[13] Diaz-Pinto, A., et al.: Monai label: a framework for ai-assisted interactive labeling of 3d medical images. arXiv preprint arXiv:2203.12362 (2022)

[14] Benabdallah N, Bernardini M, Bianciardi M, de Labriolle-Vaylet C, Franck D, Desbrée A. 223Ra-dichloride therapy of bone metastasis: optimization of SPECT images for quantification. EJNMMI Res. 2019 Feb 21;9(1):20. doi: 10.1186/s13550-019-0488-7. PMID: 30790144; PMCID: PMC6384291.

[15] Owaki Y, Nakahara T, Kosaka T, Fukada J, Kumabe A, Ichimura A, et al. Ra-223 SPECT for semi-quantitative analysis in comparison with Tc-99m HMDP SPECT: phantom study and initial clinical experience. EJNMMI Res. 2017;7:81.

[16] Lima LFC, Pinto GM, da Silva CCO, Fuser DC, Gama MP, Griebler CF, Bonifacio DAB, de Sá LV, Lopes RT. Optimal theranostic SPECT imaging protocol for 223radium dichloride therapy. J Med Imaging Radiat Sci. 2022 Sep;53(3):374-383. doi: 10.1016/j.jmir.2022.06.009. Epub 2022 Jul 16. PMID: 35850927.

[17] Xofigo. Cloreto de Rádio (223 Ra). Anvisa . Bayer Health Pharm Inc; 2018.

[18] Goceri, E. Medical image data augmentation: techniques, comparisons and interpretations. Artif Intell Rev 56, 12561–12605 (2023). https://doi.org/10.1007/s10462-023-10453-z

[19] Fedorov A, Beichel R, Kalpathy-Cramer J, Finet J, Fillion-Robin JC, Pujol S, Bauer C, Jennings D, Fennessy F, Sonka M, Buatti J, Aylward S, Miller JV, Pieper S, Kikinis R. 3D Slicer as an image computing platform for the Quantitative Imaging Network. Magn Reson Imaging. 2012 Nov;30(9):1323-41. doi: 10.1016/j.mri.2012.05.001. Epub 2012 Jul 6. PMID: 22770690; PMCID: PMC3466397.

[20] Yin XX, Sun L, Fu Y, Lu R, Zhang Y. U-Net-Based Medical Image Segmentation. J Healthc Eng. 2022 Apr 15;2022:4189781. doi: 10.1155/2022/4189781. Retraction in: J Healthc Eng. 2023 Oct 18;2023:9890389. PMID: 35463660; PMCID: PMC9033381.

[21] Isensee, F., Jaeger, P.F., Kohl, S.A.A. et al. nnU-Net: a self-configuring method for deep learning-based biomedical image segmentation. Nat Methods 18, 203–211 (2021). https://doi.org/10.1038/s41592-020-01008-z

[22] Hatamizadeh A, Tang Y, Nath V, Yang D, Myronenko A, Landman B, et al. Unetr: Transformers for 3d medical image segmentation. In: Proceedings of the IEEE/CVF Winter Conference on Applications of Computer Vision; 2022. p. 574–584.

[23] Sgouros G, Roeske JC, McDevitt MR, Palm S, Allen BJ, Fisher DR, et al. MIRD Pamphlet No. 22 (Abridged): radiobiology and dosime- try of -particle emitters for targeted radionuclide therapy. J Nucl Med . 2010;51:311–328. doi: 10.2967/jnumed.108.058651 .

[24] Grevillot L, Bertrand D, Dessy F, Freud N, Sarrut D. A Monte Carlo pencil beam scanning model for proton treatment plan simulation using GATE/GEANT4. Phys. Med. Biol. [Internet]. IOP Publishing; 2011 [cited 2018 Jan 30];56:5203–19.

[25] Costa GCA, Bonifácio DAB, Sarrut D, Cajgfinger T, Bardiès M. Optimization of GATE simulations for whole-body planar scintigraphic acquisitions using the XCAT male phantom with 177Lu-DOTATATE biokinetics in a Siemens Symbia T2. Phys. Medica [Internet]. 2017.

[26] Villoing D, Marcatili S, Garcia M-P, Bardiès M. Internal dosimetry with the Monte Carlo code GATE: validation using the ICRP/ICRU female reference computational model. Phys. Med. Biol. [Internet]. 2017;62:1885–904.

[27] Simões RFP, Da Silva CJ, Da Silva RL, Poledna R, Da Cruz PAL, De SáLV. Deconvolution method to split up X-ray peaks emitted by 223Ra. Brazilian J Radiat Sci . 2018. doi: 10.15392/bjrs.v6i1.353 .

[28] Hindorf, Cecilia; Chittenden, Sarah; Aksnes, Anne-Kirsti; Parker, Chris; Flux, Glenn D. Quantitative imaging of 223Ra-chloride (Alpharadin) for targeted alpha-emitting radionuclide therapy of bone metastases. Nuclear Medicine Communications 33(7):p 726-732, July 2012. | DOI: 10.1097/MNM.0b013e328353bb6e.

[29] Pacilio M, Ventroni G, De Vincentis G, Cassano B, Pellegrini R, Di Castro E, et al. Dosimetry of bone metastases in targeted radionuclide therapy with alpha-emitting 223Ra-dichloride. Eur J Nucl Med Mol Imaging. 2016;43:21–33. https://doi.org/10.1007/s00259-015-3150-2.

[30] Yue J, Frey EC, Mauxion T, Josefsson A, Sgouros G, Hobbs RF. Potential for quantitative imaging of Ra-223. Int J Radiat Oncol Biol Phys. 2015;93:E237.

[31] Collarino A, Pereira Arias-Bouda LM, Valdés Olmos RA, van der Tol P, Dibbets-Schneider P, de Geus-Oei LF, et al. Experimental validation of absolute SPECT/CT quantification for response monitoring in breast cancer. Med Phys. 2018;45(5):2143–53.

[32] Peters, S.M.B., Meyer Viol, S.L., van der Werf, N.R. *et al.* Variability in lutetium-177 SPECT quantification between different state-of-the-art SPECT/CT systems. *EJNMMI Phys* 7, 9 (2020). https://doi.org/10.1186/s40658-020-0278-3

[33] Goddard P, Leslie A, Jones A, Wakeley C, Kabala J. Error in radiology. Br J Radiol 2001; 74: 949–51. doi: 10.1259/bjr.74.886.740949

[34] Müller, D., Soto-Rey, I. & Kramer, F. Towards a guideline for evaluation metrics in medical image segmentation. BMC Res Notes 15, 210 (2022). https://doi.org/10.1186/s13104-022-06096-y

[35] Silosky M, Karki R, Chin BB. 68Ga and 18F quantification, and detectability of hot spots using an ACR Phantom: Contributions of radionuclide physical differences to hot spot detectability. J Nucl Med. 2019

[36] Palesi, F.; Nigri, A.; Gianeri, R.; Aquino, D.; Redolfi, A.; Biagi, L.; Carne, I.; De Francesco, S.; Ferraro, S.; Martucci, P.; et al. MRI data quality assessment for the RIN-Neuroimaging Network using the ACR phantoms. *Phys. Med. Eur. J. Med. Phys.* **2022**, *104*, 93–100

CAPÍTULO 5 - CONCLUSÃO E CONSIDERAÇÕES FINAIS

O primeiro passo para avaliar a dosimetria de lesões ósseas em pacientes com câncer de próstata resistente à castração deve ser a otimização dos parâmetros de aquisição e reconstrução. O segundo passo é avaliar a quantificação das imagens médicas e identificar a atividade nos volumes de interesse. O terceiro passo é realizar a dosimetria e avaliar a eficácia e o progresso do tratamento.

O artigo "*Optimal theranostic SPECT imaging protocol for 223radium dichloride therapy*" demonstrou que os parâmetros de aquisição recomendados de matriz 128 × 128, colimador LEHR e fotopico centralizado em 89 keV (largura de 24%) podem ser utilizados para a aquisição SPECT de imagens de dicloreto de rádio 223. Adicionalmente, OSEM/MLEM com 4 iterações e o filtro Butterworth (frequência de corte de 0,48 ciclos/cm-1 e ordem 10) foi o parâmetro de reconstrução com o melhor desempenho. Além disso, embora o uso do colimador LEHR exija mais testes comparativos, o colimador LEHR permitiu a visualização e quantificação de todos os parâmetros de qualidade da imagem, portanto é considerado uma possibilidade confiável em estudos futuros.

O artigo "*Radium-223 Dosimetry through Monte Carlo simulation and Deep Learning-Based Jaszczak ACR Phantom Segmentation"*, submetido à publicação demonstrou a superioridade da janela de 89 keV (largura de 24%) em comparação as outras janelas de energia através da avaliação dos parâmetros de qualidade de imagem. Além disso, a quantificação das imagens e a análise dosimétrica demonstraram a importância do uso do Coeficiente de Recuperação na atividade e nos valores de dose absorvida de diversos tamanhos de volumes de interesse. Portanto, a correção dos efeitos de volume parcial é necessária, uma vez que a quantificação de lesões menores pode resultar em subestimação de até 74% na avaliação da dose absorvida. Além disso, o estudo introduziu um modelo de inteligência artificial para segmentação automática das áreas captantes do simulador Jaszczak ACR, mostrando sua potencial aplicabilidade em várias modalidades de imagens médicas e sua maior eficiência no protocolo dosimétrico.

Este estudo não só contribui com avanços significativos para o refinamento dos protocolos de dosimetria em terapias com Ra-223 em MN, mas também oferece implicações práticas para melhorar a precisão dos resultados quantitativos, especialmente em cenários que envolvem estruturas de tamanhos variados.

CAPÍTULO 6 - DIREÇÕES FUTURAS

Os próximos passos da pesquisa nesta área podem se concentrar no refinamento e otimização do protocolo de imagem SPECT para exames de rádio-223. O presente estudo enfatizou a utilização da janela de energia de 89 keV (24%), demonstrando sua superioridade em termos de parâmetros de qualidade de imagem e valores de contraste em comparação com outras janelas de energia propostas na literatura. Estudos comparativos, utilizando a janela de 89 keV (24%), entre os tipos de colimadores, LEHR, MEGP e HEGP, podem fornecer informações valiosas sobre sua adequação para imagens de rádio-223, especialmente no contexto de diferentes tamanhos de lesões.

Pesquisas futuras devem priorizar o desenvolvimento e avaliação de técnicas destinadas a mitigar os efeitos de volume parcial em imagens de medicina nuclear. Isto poderia envolver algoritmos de reconstrução, métodos avançados de processamento de imagem ou incorporação do coeficiente de recuperação.

O estudo enfatizou o potencial para melhorias sistemáticas, incluindo a integração de segmentação automatizada e técnicas de inteligência artificial, para reduzir significativamente o percentual de erro e aumentar a eficiência do fluxo de trabalho. A investigação futura deverá centrar-se no avanço destas técnicas, com especial ênfase na sua aplicação clínica. Podem ser exploradas estratégias de colaboração entre ferramentas de segmentação automatizadas e especialistas clínicos para garantir a personalização e o refinamento dos modelos de segmentação.

Pesquisas futuras deverão ter como objetivo validar e padronizar técnicas de quantificação, especialmente no contexto da análise dosimétrica. Abordar as variações nos valores das doses devido às técnicas de reconstrução é crucial para garantir a confiabilidade e a comparabilidade dos resultados entre os estudos. O estabelecimento de protocolos padronizados para análise dosimétrica contribuirá para a precisão e consistência das aplicações da medicina nuclear. Esta estratégia padronizada contribuirá para o avanço do campo da medicina nuclear, melhorando a precisão das aplicações diagnósticas e terapêuticas.

REFERÊNCIAS

ALGETA. **Focused on the development of novel targeted cancer therapeutics. Annual Report of 2010**. Highlights of 2010. 2010. Disponível em : <https://www.annualreports.com/HostedData/AnnualReportArchive/b/OTC_BAYZF_2010.pdf>.

ASSIÉ, K. *et al.* **Monte Carlo simulation in PET and SPECT instrumentation using GATE**. Nucl. Instrum. Methods Phys. Res. a 2004.

ATKINS, H. L. **Overview of nuclides for bone pain palliation. A*pplied Radiation and Isotope.***, 1998. v. 49, n. 4, p. 277-283.

BAYER, H. **Product monograph - XOFIGO**. p. 1–29, 2015. Disponível em: <https://www.bayer.com/sites/default/files/xofigo-pm-en.pdf >.

BAYER, H. **Xofigo: Cloreto de Rádio (223 Ra)**. Anvisa, Bayer Healthc. Pharm. Inc, 2018.

BEER, T. M. *et al*. **Enzalutamide in men with chemotherapy-naive metastatic castration-resistant prostate cancer: extended analysis of the phase 3 PREVAIL study.** Eur Urol. 2017;71:151–4.

BENABDALLAH, N. M.; BERNARDINI, M. *et al*. **223 Ra-dichloride therapy of bone metastasis: optimization of SPECT images for quantification.** *EJNMMI Res*., 2019.

BONIFACIO, D. A. B. **Validação do Geant4 para a produção e detecção de raios-X na faixa de energia de radiodiagnóstico.** Dissertação de mestrado. Dissertação (Mestrado) - Instituto de física, São Paulo, 2007.

BOLCH, W. E. et al. **MIRD pamphlet No. 17: the dosimetry of nonuniform activity distributions--radionuclide S values at the voxel level**. Medical Internal Radiation Dose Committee. J. Nucl. Med., vol. 40, no. 1, pp. 11S-36S, 1999.

BRITO, A. E.; ETCHEBEHERE, E. *et al.* **Radium-223 as an Approved Modality for Treatment of Bone Metastases**. Semin Nucl Med. 2020 Mar;50(2):177-192. doi: 10.1053/j.semnuclmed.2019.11.005. Epub 2020 Mar 11. PMID: 32172803.

BRULAND, Ø. S.; NILSSON, S.; FISHER, D. R; *et al.* **High-Linear Energy Transfer Irradiation Targeted to Skeletal Metastases by the α-Emitter 223Ra: Adjuvant or Alternative to Conventional Modalities?** *Clinical Cancer Research*, v. 12, n. 20, p.6250s--6257s, 2006.

BUBENDORF, L. *et al*. **Metastatic patterns of prostate cancer: an autopsy study of 1,589 patients.** Hum Pathol. 2000 May;31(5):578-83. doi: 10.1053/hp.2000.6698. PMID: 10836297.

BUCHALI, K.; CORRENS, H. J.; SCHUERER, M. *et al*. **Results of a double blind study of 89-strontium therapy of skeletal metastases of prostatic carcinoma**. Eur J Nucl Med. 1988;14:349–351.

BUSHBERG, J.T., SEIBERT, J. A., LEITHOLDT, E.M. **The essential physics of medical imaging**. 3rd ed. Philadelphia, PA: Lippincott Williams & Wilkins; 2012.

BYBEL, B. *et al.* **Spect/ct imaging: Clinical utility of an emerging technology.** RadioGraphics, v. 28, n. 4, p. 1097–1113, 2008. PMID: 18635631. Disponível em: <https://doi.org/10.1148/rg.

CARRASQUILLO, J. A.; O'DONOGHUE, J. A.; PANDIT-TASKAR, N. *et al*. **Phase I pharmacokinetic and biodistribution study with escalating doses of 223Radichloride in men with castration-resistant metastatic prostate cancer.** *European Journal of Nuclear Medicine and Molecular Imaging*, v. 40, n. 9, p. 1384–1393, 2013.

CHAHBOUB, Y. *et al*. **Assessment of absorbed dose by target organs using mird formalism during certain nuclear medicine procedures.** Euro Journal of Biomedical and Pharmaceutical Sciences, 3 (2016), pp. 61-6.

CHITTENDEN, S. J.; HINDORF, C.; PARKER, C. C.; *et al.* **A Phase 1, Open-Label Study of the Biodistribution, Pharmacokinetics, and Dosimetry of 223Ra-Dichloride in Patients with Hormone-Refractory Prostate Cancer and Skeletal Metastases**. Journal of Nuclear Medicine, v. 56, n. 9, p. 1304–1309, 2015.

CLARE, C. *et al*. **Painful bone metastases: a prospective observational cohort study**. *Palliative Medicine*, v. 19, n. 7, p. 521-525. 2005.

COLLINS, S. M. *et al*. **Precise measurements of the absolute X-ray emission probabilities of 223 Ra and decay progeny in equilibrium.** *Applied Radiation and Isotopes*, v. 102, p. 15-28. 2015.

COSENTINO, M. R. **Simulation for high energy physics detectors**. ICTP-SAIFR/FAIR Workshop on Mass Generation in QCD 27/February/2019.

DANIELI, R. *et al.* **Personalized Dosimetry in Targeted Radiation Therapy: A Look to Methods, Tools and Critical Aspects**. J Pers Med. 2022 Feb 2;12(2):205. doi: 10.3390/jpm12020205. PMID: 35207693; PMCID: PMC8874397.

DE BONO, J. S. *et al*. S**ubsequent chemotherapy and treatment patterns after abiraterone acetate in patients with metastatic castration resistant prostate cancer: post hoc analysis of COU-AA-302**. Eur Urol. 2017;71:656–64.

DEWARAJA, Y. K. *et al.* **MIRD Pamphlet No. 23: Quantitative SPECT for Patient-Specific 3-Dimensional Dosimetry in Internal Radionuclide Therapy**. J. Nucl. Med., vol. 53, no. 8, pp. 1310–1325, 2012.

DOI, K. **Computer-aided diagnosis in medical imaging: historical review, current status and future potential**. Comput Med Imaging Graph. 2007;31:198–211.

D'ARIENZO, M.; *et al*. **Gamma camera calibration and validation for quantitative SPECT imaging with (177)Lu.** Appl Radiat Isot Incl Data, Instrum Methods Use Agric Ind Med. 2016;112:156–64. https://doi.org/10.1016/j.apradiso.2016.03.007.

ECHEGARAY, S.; GEVAERT O, SHAH R, *et al*. **Core samples for radiomics features that are insensitive to tumor segmentation: method and pilot study using CT images of hepatocellular carcinoma**. Journal of Medical Imaging (Bellingham). 2015.

ERICKSON, B. J. *et al.* **Machine learning for medical imaging.** Radiographics. 2017;37:505–15.

EISBERG, R. e RESNICK., R. **Física Quântica**. Editora Campus Ltda. 1979.

FDA U. **Highlights of prescribing information.** https://www.accessdata.fda.gov/drugsatfda_docs/label/2013/203971lbl.pdf.

FLUX, G. D., 2017, **Imaging and dosimetry for radium-223: the potential for personalized treatment.** The British Journal of Radiology, v. 90, n. 0, p. 20160748.

GARTNER, L. P. e HIATT, J. L. **Histologia básica**. Edição 1, *Elsevier, Brasil*, 2011, pp.156.

GIGER, M. L. **Machine learning in medical imaging**. Journal of the American College of Radiology; 2018.

GILLIES, R.J.; KINAHAN, P. E.; HRICAK, H. **Radiomics: images are more than pictures, they are data**. Radiology. 2016.

GOODFELLOW, I.; BENGIO, Y.; COURVILLE, A. **Deep learning**. MIT Press. 2016.

GONZALEZ, R.C.; e WOODS R. E**. Digital image processing**. Upper Saddle River, NJ: Prentice Hall; 2007.

GUISE, T. A.; MOHAMMAD, K. S.; CLINES, G.; *et al*. **Basic mechanisms responsible for osteolytic and osteoblastic bone metastases**. *Clinical Cancer Research*, v. 12, n. 20 PART 2, p. 6213–6217, 2006.

HAYKIN, S. **Neural networks: a comprehensive foundation**. Upper Saddle River, NJ: Prentice Hall; 1994.

HINDORF, C. *et al*. **Quantitative imaging of 223Ra-chloride (Alpharadin) for targeted alpha-emitting radionuclide therapy of bone metastases.** *Nuclear medicine communications*. 33. 726-32. 2012.

INCA, Instituto Nacional de Câncer. **Estimativa 2023: Incidência de Câncer no Brasil.** Rio de Janeiro. Brasil. 2022.

KAIREMO, K.; JOENSUU, T.; RASULOVA, N. et al. **Evaluation of Alpha-Therapy with Radium-223-Dichloride in Castration Resistant Metastatic Prostate Cancer—the Role of Gamma Scintigraphy in Dosimetry and Pharmacokinetics.** Diagnostics, v. 5, n. 3, p. 358–368, 2015.

KANTOFF, P. W. *et al*. **Sipuleucel-T immunotherapy for castration-resistant prostate cancer**. N Engl J Med. 2010;363:411–22.

KLUETZ, P. G.; PIERCE, W.; MAHER, V. E.; *et al*. **Radium Ra-223 Dichloride Injection: U.S. Food and Drug Administration Drug Approval Summary**. *Clinical Cancer Research*, v. 20, n. 1, p. 9–14, 2014.

KNOLL, G. F., **Radiation Detection and Measurement**, Vol. 3. 2010.

LARSEN, R. H.; SAXTORPH, H.; SKYDSGAARD, M. et al. **Radiotoxicity of the alpha-emitting bone-seeker 223Ra injected intravenously into mice: Histology, clinical chemistry and hematology.** In Vivo, v. 20, n. 3, p. 325–332, 2006.

LAZARO, D. *et al*. **Fully 3D Monte Carlo reconstruction in SPECT: a feasibility study.** Phys Med Biol. 2005 Aug 21;50(16):3739-54. doi: 10.1088/0031-9155/50/16/006. Epub 2005 Jul 28. PMID: 16077224.

LEWINGTON, V. J. **Bone-seeking radionuclides for therapy.** J*ournal of Nuclear Medicine*, 2005. v. 46, n. 1 suppl, p. 38S-47S.

LIEN, L. E. *et al* **Treatment of castration-resistant prostate cancer and bone metastases with radium-223 dichloride.** I*nternational Journal of Urological Nursing*, v. 9, n. 1, p. 3–13, 2015.

LJUNGBERG, M. *et al*. **MIRD pamphlet no. 26: Joint eanm/mird guidelines for quantitative 177lu SPECT applied for dosimetry of radiopharmaceutical therapy.** Journal of Nuclear Medicine, v. 57, n. 1, p. 151–162, 2016.

MACEDO, F. et al. **Bone metastases: An overview.** Oncol. Rev., vol. 11, no. 1, 2017.

MADSEN, M. T. **Recent advances in SPECT imaging.** J Nucl Med. 2007 Apr;48(4):661-73. doi: 10.2967/jnumed.106.032680. PMID: 17401106.

MARQUES, I. A. *et al*.**Targeted alpha therapy using Radium-223: From physics to biological effects**. (2018) Cancer treatment reviews, 68, 47-54.

MASTRO, A. M. *et al*. **The skeleton as a unique environment for breast cancer cells.** *Clinical and Experimental Metastasis*, v. 20, n. 3, p. 275–284, 2003.

MCPARLAND, B. J.; **Nuclear Medicine Radiation Dosimetry: Advanced Theoretical Principles**. London, 2010.

MEISEL, A. *et al* **Severe neutropenia during cabazitaxel treatment is associated with survival benefit in men with metastatic castration-resistant prostate cancer (mCRPC): a post-hoc analysis of the TROPIC phase III trial**. Eur J Cancer. 2016;56:93–100.

MOSTAFA, B. *et al*. **Machine and Deep Learning Approaches in Genome: Review Article.** 2021 *Alfarama Journal of Basic & Applied Sciences*, *2*(1), 105-113. doi: 10.21608/ajbas.2020.34160.1023

MORRIS, M. J. *et al.* **Radium-223 mechanism of action: implications for use in treatment combinations**. Nat Rev Urol 16, 745–756 (2019). https://doi.org/10.1038/s41585-019-0251-x.

MUNDY, G. R. *et al.* **Metastasis to bone: causes, consequences and therapeutic opportunities**. *Nature Reviews Cance*r, v. 2, p. 584, 1 ago. 2002.

NICHOLS, A. L. *et al*. **Table of radionuclides (Vol. 6–A= 22 to 242).** Monographie BIPM-5, Bureau International des Poids et Mesures, Sèvres. pp.95-103. 2011.

NILSSON, S.; LARSEN, R. H.; FOSSA, S. D. *et al.* **First clinical experience with alpha-emitting radium-223 in the treatment of skeletal metastases.** Clin Cancer Res. 2005;11:4451–445.

OSTUNI, E. *et al*. **Commercial and business aspects of alpha radioligand therapeutics**. Front Med (Lausanne). 2023 Feb 2;9:1070497. doi: 10.3389/fmed.2022.1070497. PMID: 36816719; PMCID: PMC9932801.

OWAKI, Y. *et al* **Ra-223 SPECT for semi-quantitative analysis in comparison with Tc-99m HMDP SPECT: phantom study and initial clinical experience.** EJNMMI Res. 2017 Oct 3;7(1):81. doi: 10.1186/s13550-017-0330-z. PMID: 28975570; PMCID: PMC5626671.

PACILIO, M. *et al.* **Physica Medica The Italian multicentre dosimetric study for lesion dosimetry in 223 Ra therapy of bone metastases : Calibration protocol of gamma cameras and patient eligibility criteria**. Phys. Medica, vol. 32, no. 12, pp. 1731–1737, 201. 2016.

PANDIT-TASKAR, N.; LARSON, S. M.; CARRASQUILLO, J. A. *et al* **Bone-Seeking Radiopharmaceuticals for Treatment of Osseous Metastase, Part 1: α Therapy with 223Ra-Dichloride**. *The Journal of Nuclear Medicine*, 2014.

PARKER, C.; NILSSON, S.; HEINRICH, D. *et al.* **Alpha emitter radium-223 and survival in metastatic prostate cancer**. New England Journal of Medicine. 2013;369: 213– 23.

PARKER, C. *et al*. **Current approaches to incorporation of radium-223 in clinical practice**. Prostate Cancer Prostatic Dis. 2018;21:37–47.

PARKER, J. **Algorithms for image processing and computer vision**. 2nd ed. Wiley; 2011.

RITTER, M. A. *et al*. **High-LET radiations induce a large proportion of non-rejoining DNA breaks.** *Nature,* v. 266, n. 5603, p. 653–655, 1977. Disponível em: <https://doi.org/10.1038/266653a0>.

ROODMAN, G. D. **Mechanisms of bone metastasis.** ***New England Journal of Medicine***, v. 350, n. 16, p. 1655-1664. 2004.

RYAN, C. J. et al. **Abiraterone acetate plus prednisone versus placebo plus prednisone in chemotherapy-naive men with metastatic castration resistant prostate cancer (COU-AA-302): final overall survival analysis of a randomized, double-blind, placebo-controlled phase 3 study.** Lancet Oncol. 2015;16:152–60.

SADI, M. V. *et al.* **Câncer da próstata resistente à castração (CPRC)**. Comitê Brasileiro de Estudos em Uro-Oncologia (CoBEU), v. 25, 2011.

SAHA, G. B. **Basics of PET imaging: Physics, chemistry, and regulations.** 3rd edition. New York: Springer, 2016.

SARRUT, D. *et al.* **A review of the use and potential of the GATE Monte Carlo simulation code for radiation therapy and dosimetry applications**. Medical Physics, v. 41, n. 6, 2014.

SARTOR, O.; REID, R.H.; HOSKIN, P.J. *et al.* **Samarium-153-lexidronam complex for treatment of painful bone metastases in hormone-refractory prostate cancer**. Urology. 2004;63:940–945.

SCARINCI, I.; VALENTE, M.; PÉREZ, P. *et al* **Dose Point Kernel calculation and modeling with nuclear medicine dosimetry purposes.** Proc. Sci., no. December, pp. 1–6, 2013.

SERAFINI, A.N.; HOUSTON, S. J. *et al.* **Palliation of pain associated with metastatic bone cancer using samarium-153 lexidronam: A double-blind placebo-controlled clinical trial.** J Clin Oncol. 1998;16:1574–1581.

SIMÕES, R. F. P. **Padronização Absoluta do Ra-223 e Calibração dos Sistemas de Referência do LNMRI.** IRD - Radioprotection and Dosimetry Institute, 2018.

SGOUROS, G.; ROESKE, J. C.; MCDEVITT, M. R. *et al*. **MIRD Pamphlet No. 22 (Abridged): Radiobiology and Dosimetry of α-Particle Emitters for Targeted Radionuclide *Therapy***. *Journal of Nuclear Medicine*, v. 51, n. 2, p. 311–328, 2010.

SGOUROS, G. e HOBBS R. F. **Dosimetry for radiopharmaceutical therapy**. *Semin. Nucl. Med.*, vol. 44, no. 3, pp. 172–178, 2014.

SONG, X.; SEGARS, W. P. *et al*. **Fast modelling of the collimator-detector response in Monte Carlo simulation of SPECT imaging using the angular response function**. Physics in Medicine and Biology, v. 50, n. 8, p. 1791, 2005.

SONKA, M.; HLAVAC, V.; BOYLE, R. **Image processing, analysis and machine vision.** Boston, MA: Springer; 1993.

STABIN, M. G. **The Practice of Internal Dosimetry in Nuclear Medicine**. Florida: CRC Press, Taylor & Francis Group, 2017.

SUNG, *et al*., **Global Cancer Statistics 2020:GLOBOCAN Estimates of Incidence and mortality Worldwide for 3 Cancers in 185 Countrie.**, *ACS Journals*, 2021.

TANNOCK, I. F. *et al.* **Docetaxel plus prednisone or mitoxantrone plus prednisone for advanced prostate cancer**. *New England Journal of Medicine* 351.15, pp.1502-1512. 2004.

TANTIVEJKUL, K. *et al.* **Dynamic process of prostate cancer metastasis to bone.** *Journal of Cellular Biochemistry*, v. 91, n. 4, p. 706–717, 2004.

TUNCEL M.; TUNCALI M. *et al*. **Clinical Impact of PET Imaging in Patients With Metastatic Prostate Cancer**. Clin Nucl Med. 2020 Oct;45(10):757-764. doi: 10.1097/RLU.0000000000003126. PMID: 32701793.

VIEIRA, S. C.*et al*. **Oncologia Básica**. 1a ed. Teresina, PI, BRA: Fundação Quixote, 2012.

VIRK, M. S.; LIEBERMAN, J. R. **Tumor metastasis to bone. Arthritis research & therapy**, v. 9 Suppl 1, n. Suppl 1, p. S5–S5, 2007.

ZAIDI, H. **Quantitative Analysis in Nuclear Medicine Imaging**. Springer Nature Springer. 2006.

WERNICK, M. N. and AARSVOLD J.N. Emission Tomography - **The Fundamentals of PET and SPECT**. Elsevier, 2004. Disponível em : <https://www.sciencedirect.com/book/9780127444826/emission-tomography>

WHO, World Health Organization. **Report on Cancer: Setting Priorities, Investing Wisely and Providing Care for All.** Technical Report; World Health Organization: Geneva, Switzerland, 2020.